sensors

MDPI

Article

Use of a Force-Torque Sensor for Self-Calibration of a 6-DOF Medical Robot

Ahmed Joubair *, Long Fei Zhao, Pascal Bigras and Ilian A. Bonev

École de Technologie Supérieure (ÉTS), Montreal, QC H3C 1K3, Canada; longfei.zhao.1@ens.etsmtl.ca (L.F.Z.); pascal.bigras@etsmtl.ca (P.B.); ilian.bonev@etsmtl.ca (I.A.B.)

* Correspondence: ahmed.joubair.1@ens.etsmtl.ca; Tel.: +1-514-895-8117

Academic Editor: Vittorio M. N. Passaro

Received: 2 March 2016; Accepted: 26 May 2016; Published: 31 May 2016

Abstract: The aim of this paper is to improve the position accuracy of a six degree of freedom medical robot. The improvement in accuracy is achieved without the use of any external measurement device. Instead, this work presents a novel calibration approach based on using an embedded force-torque sensor to identify the robot's kinematic parameters and thereby enhance the positioning accuracy. A simulation study demonstrated that our calibration approach is effective, whether or not any measurement noise is present: the position error is improved, inside the robot target workspace, from 12 mm to 0.320 mm, for the maximum values, and from 9 mm to 0.2771 mm, for the mean errors.

Keywords: robot calibration; robot accuracy; observability; medical robot; robot kinematic; robotic metrology

1. Introduction

Medical robots show a promising future in various health issues in the most recent decades. With recent developments in sensors and control theory, medical robots provide many inspiring solutions in the fields of: diagnosis, surgery, orthopedics, rehabilitation, prosthetics and exoskeletons, *etc.* [1,2]. The force-torque (wrench) sensor is an essential component of these medical robot applications. MedRUE [3], OTELO [4] and Hippocrate [5] robot systems were developed for the ultrasound scanning of vascular diseases. In all three robot systems, force-torque sensors are employed to maintain proper contact with the patient's body during the examination. The Black Falcon system, which is a fundamental study for many other surgical robot systems, allows the surgeon to feel the interaction with tissue and thereafter improve the surgical performance. The Da Vinci system is a popular surgery robot widely used in hospitals [6]. The adoption of force-torque sensors in Da Vinci system has been studied in depth [7]. The Robodoc assistant system is a medical orthopedic robot for use during total knee replacement, and it achieves results that are comparable to technician performance [8]. The force-torque sensors are used in Robodoc for both control and safety reasons.

Medical robots have also contributed to the field of rehabilitation. The InMotion ARM, which is based on the MIT-Manus project, is an interactive robotic system for upper-extremity rehabilitation therapy [9,10], and the robotic stepper is a device, developed by the National Aeronautics and Space Administration (NASA), to help patients with lower-extremity rehabilitation [11]. Force-torque sensors are employed in these rehabilitation robots to measure the strength and the capability of the patient. Medical robots have also been developed as substitutes for malfunctioning parts of the human body. The I-limb ultrasound system and the ReWalk system are exoskeleton robots for hand prosthetics and leg prosthetics, respectively [12,13]. Force-torque sensors are used in the prosthetic and exoskeleton robots to control the joints and to evaluate the power of the limb movements.

Medical robots often need to be accurate, not just repeatable, which means that they must be calibrated. Most robot calibration approaches are based on minimizing the pose residual, which

involves external measurement devices such as a coordinate measurement machine (CMM) [14,15], laser tracker [16–18], measurement articulated arm [14], ball-bar [19,20], or a high-accuracy touch probe [21,22]. However, these measurement devices tend to be expensive, and they are not readily available. Furthermore, even though other studies have developed low-cost calibration methods, such as in [19,20], they still require the use of external measurement devices.

Other robotic applications are dedicated to measuring and/or reproducing human movements, such as [23], which presents a methodology to accurately record human finger postures during grasping. In this work, human finger postures are measured during grasping. As with the aforementioned works, measurements are taken with external measurement devices: an optical tracking of markers that are attached to the skin of the hand, and tracked using stereo-cameras. The considered kinematic parameters in this work are geometric static parameters, and parameters controlling the location of the bones and the joint markers. These parameters are identified by using a constrained least-squares minimization. The minimization problem is solved by employing a primal-dual interior point. It minimizes the residuals of the coordinates of measured markers and the corresponding estimated coordinates, which are a function of the static parameters and joint angle values.

Force-torque sensors are already used in many medical robot systems, so it makes sense to use these sensors, rather than external coordinate measurement equipment, for calibrating the robots (*i.e.*, improving the robot positioning accuracy). Yet, to the best of our knowledge, no such calibration methods have been proposed in the literature. In previous work, other measurement approaches were used, such as Cartesian coordinates [14–18], or distance measurements [19,20]. The novelty of our work is the use of a force-torque sensor to improve the positioning accuracy of a medical robot (MedRUE). The robot parameters are identified by minimizing the force and torque residuals, instead of minimizing the residuals of the end-effector position and/or orientation, as done in conventional approaches [14–20]. The sensor we used is the embedded force-torque sensor, located between the flange and the tool. Thus, our calibration approach can be considered as a self-calibration method.

The proposed approach could be used for any other medical or industrial robot. Industrial robots are not always equipped with force-torque sensors. However, such sensors are readily available in the market and can be easily installed. Indeed, industrial serial robots are increasingly using these sensors for programming purposes: the force-torque sensors are installed in order to move manually the robot end-effector, during the online programming (also called lead-through programming).

In the identification process proposed in this paper, the data are collected by the robot's force-torque sensor. The process of identifying the parameters is based on minimizing the residual of the force and torque at the robot's end-effector. The accurate identification of the robot's parameters leads to improved position accuracy. Our approach is validated through a simulation, in which the position accuracy is evaluated before and after calibration.

This paper is organized as follows. The next section describes the force and torque forward kinematic equations, followed by a description of the calibration approach. We then present our simulation study, followed by a results analysis. Finally, we discuss our conclusions and suggestions for further work in the last section of the paper.

2. Robot Description and Forward Kinematics

2.1. Robot Description and the Main Reference Frames

The MedRUE robot (Figure 1a) is a medical robot dedicated for vascular ultrasound examination. MedRUE is a six degrees of freedom (6-DOF) hybrid serial-parallel robot. It is composed of two five-bar mechanisms (Figure 1b), which are symmetrically assembled. These mechanisms are considered to be perfectly parallel to each other and perpendicular to the robot base. The robot base is fixed to a linear guide actuated through a servomotor SM_1; the corresponding joint variable is denoted by q_1. Five other servomotors are also used in order to actuate the robot revolute joints: SM_2 and SM_3, for the left five bar mechanism, and SM_4 and SM_5 for the right side (Figure 1a). The sixth servomotor—attached

to the link having L_{14} as its length—is used to rotate the probe about the x axis of the last reference frame (F_6), which is defined as follows: the origin of F_6 is located midway between G_1 and G_2; its x axis (x_6) is defined to pass through G_1 and G_2, and z_6 is pointing toward the probe center.

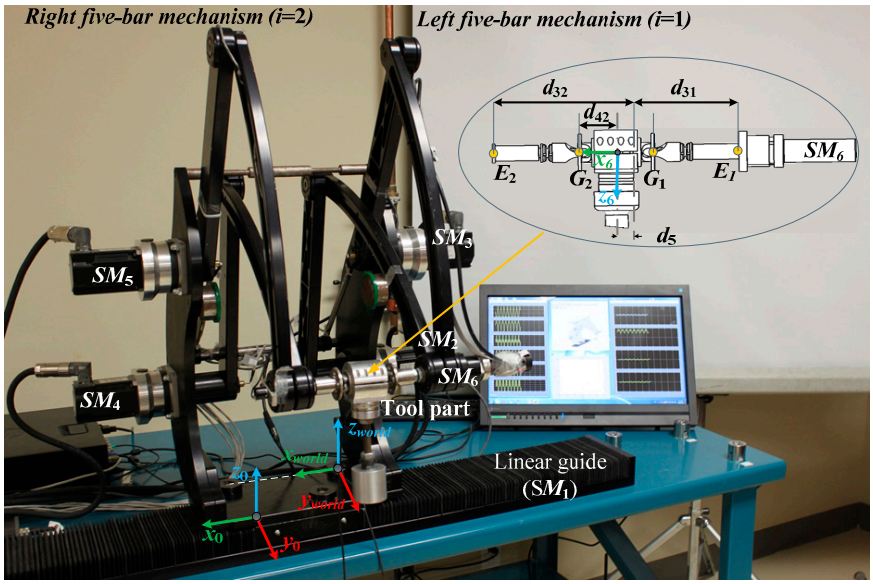

(**a**)

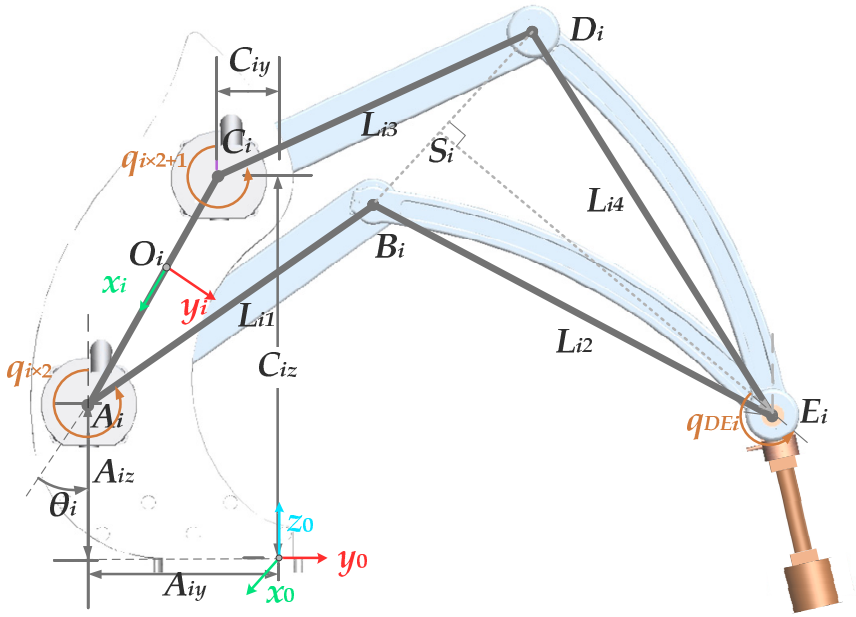

(**b**)

Figure 1. (**a**) The MedRUE robot prototype with the tool part and (**b**) a five-bar mechanism of the MedRUE where (i = 1, 2).

Each five-bar mechanism i (i = 1, 2) has five links: the distance d_i between the anchor points of the two proximal links, and the four mobile links having L_{ij} (j = 1, 2, 3, 4) as lengths. The five links connect five revolute joints (A_i, B_i, C_i, D_i, E_i), among which only two (A_i and C_i) are actuated through servomotors $SM_{i\times2}$ and $SM_{i\times2+1}$: the corresponding two angles are denoted $q_{i\times2}$ and $q_{i\times2+1}$, respectively. A total of five angles of active joints are considered (q_2, ... , q_6).

Finally, joints E_1 and E_2 are linked through the probe support (Figure 1a), which has a universal joint at each extremity G_i. The x coordinate of G_i with respect to the base frame is denoted by d_{4i}.

In our calibration process, nine reference frames are considered:

- F_0: The reference frame of the robot base, located on the robot base at O_0. As shown in Figure 1a, the x axis (x_0) is aligned with the axis of the linear guide, and z_0 is normal to the plane defined by the platform of the robot base. The translation $\mathbf{T}_0^{world} = \begin{bmatrix} x_0 & y_0 & z_0 \end{bmatrix}^T$ and the orientation (α_0, β_0, γ_0), described in XYZ fixed Euler angles, of F_0 with respect to F_{world}, are expected to be identified by the calibration process.
- F_{world}: The world reference frame (Figure 1a), associated with the robot work-cell. It has approximately the same orientation as F_0.
- F_1 to F_6: The reference frames associated with the joints (F_1, F_2, ... , F_6). These frames are not shown.
- F_{tool}: The tool reference frame associated with the robot probe (Figure 2). The origin of F_{tool} is described to be the center of the end-effector (*i.e.*, the probe), and its orientation is considered to be the same as that of F_6. Knowing that the end-effector orientation is not used in our calibration process, therefore, only the translation $\mathbf{T}_{\text{tool}}^{6} = \begin{bmatrix} x_t & y_t & z_t \end{bmatrix}^T$ of F_{tool} with respect to F_6 is considered.

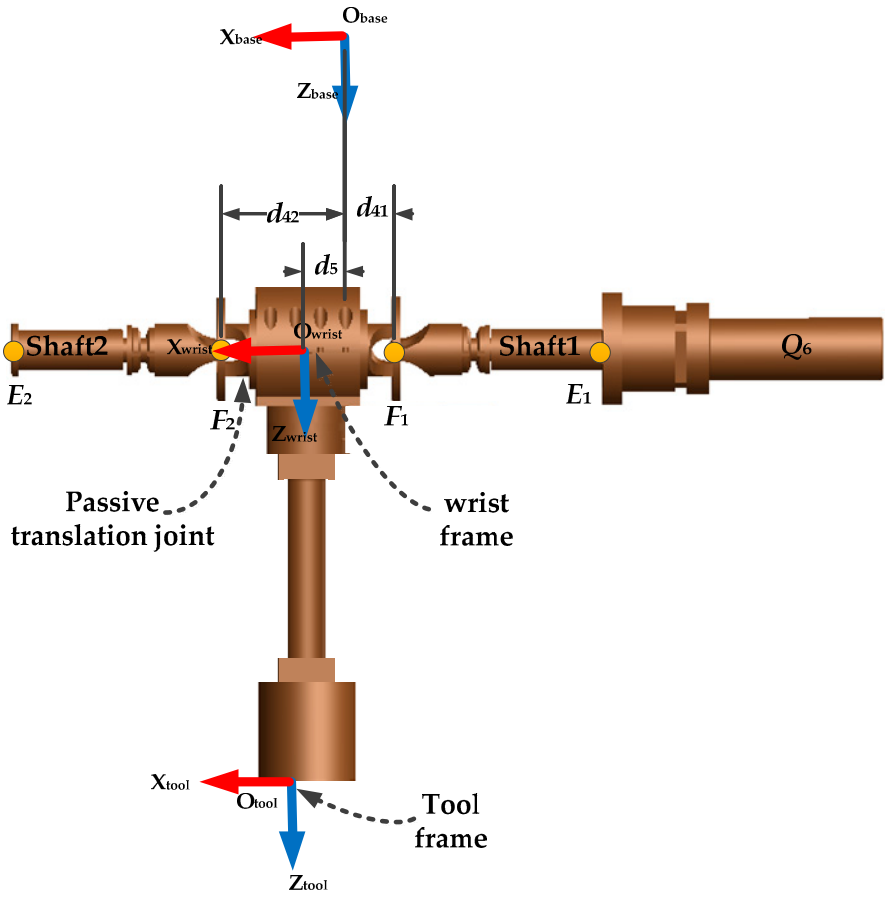

Figure 2. Tool part of MedRUE.

2.2. Position Equations

Given the vector $\psi = [q_1, q_2, \ldots, q_6]^{\mathrm{T}}$ of the active joint variables, the end-effector's pose with respect to the world frame is represented by homogeneous matrices as follows:

$$\mathbf{A}_{\text{tool}}^{\text{world}}(\psi) = \mathbf{A}_{\text{base}}^{\text{world}}\mathbf{A}_{\text{wrist}}^{0}\mathbf{A}_{\text{sensor}}^{\text{wrist}}\mathbf{A}_{\text{tool}}^{\text{sensor}} \quad (1)$$

where $\mathbf{A}_a^b$ denotes the homogeneous matrix representing a frame a with respect to a frame b, and can be represented in the matrix form of $\begin{bmatrix} \mathbf{R}_a^b & \mathbf{T}_a^b \\ \mathbf{0} & 1 \end{bmatrix}$.

The rotation matrix is often represented by $\mathbf{R}(\alpha,\beta,\gamma) = \mathbf{R}_x(\gamma)\mathbf{R}_y(\beta)\mathbf{R}_z(\alpha)$, and the translation matrix by $\mathbf{T}(x,y,z) = \mathbf{T}_x(x)\mathbf{T}_y(y)\mathbf{T}_z(z)$, where $\mathbf{R}_u(\phi)$ and $\mathbf{T}_u(d)$ are the rotation/translation operator along the u axis with value ϕ/d. Since robot joints are only included in $\mathbf{A}^0_{\text{wrist}}$, then $\mathbf{A}^{\text{world}}_{\text{base}}$, $\mathbf{A}^{\text{wrist}}_{\text{sensor}}$ and $\mathbf{A}^{\text{sensor}}_{\text{tool}}$ in Equation (1) are constant matrices, which can be defined directly by parameter sets [x_0, y_0, z_0, α_0, β_0, γ_0], [x_S, y_S, z_S, α_S, β_S, γ_S] and [x_T, y_T, z_T, α_T, β_T, γ_T]. The following paragraphs present the calculation of $\mathbf{A}^0_{\text{wrist}}$.

The coordinates of B_i and D_i are expressed with respect to the local frame F_i on ith five-bar mechanism as follows:

$$\mathbf{r}_{O_iB_i} = \mathbf{r}_{O_iA_i} + \begin{bmatrix} L_{i1}\cos(q_{i\times2} + \delta q_{i\times2}) & L_{i1}\sin(q_{i\times2} + \delta q_{i\times2}) & 0 \end{bmatrix}^T \tag{2}$$

$$\mathbf{r}_{O_iD_i} = \mathbf{r}_{O_iC_i} + \begin{bmatrix} L_{i3}\cos(q_{i\times2+1} + \delta q_{i\times2+1}) & L_{i3}\sin(q_{i\times2+1} + \delta q_{i\times2+1}) & 0 \end{bmatrix}^T \tag{3}$$

where L_{i1} and L_{i3} are the lengths of the four swinging links as shown in Figure 1, and δq_i is the offset of ith active joint. The vector $\mathbf{r}_{O_iA_i}$ is calculated as follows:

$$\mathbf{r}_{O_iA_i} = \begin{bmatrix} \frac{\sqrt{(C_{iy}-A_{iy})^2+(C_{iz}-A_{iz})^2}}{2} & 0 & 0 \end{bmatrix}^T \tag{4}$$

and

$$\mathbf{r}_{O_iC_i} = -\mathbf{r}_{O_iA_i} \tag{5}$$

The coordinates of E_i with respect to a frame F_i are obtained as follows:

$$\mathbf{r}_{O_iE_i} = \mathbf{r}_{O_iD_i} + \mathbf{r}_{D_iS_i} + \mathbf{r}_{S_iE_i} \tag{6}$$

where

$$\mathbf{r}_{D_iS_i} = \frac{\mathbf{r}_{D_iB_i}}{2}\left(\frac{L_{i4}^2 - L_{i2}^2}{||\,\mathbf{r}_{D_iB_i}\,||^2} + 1\right) \tag{7}$$

$$\mathbf{r}_{S_iE_i} = \sqrt{L_{i4}^2 - ||\,\mathbf{r}_{D_iS_i}\,||^2}\,\mathbf{R}_z\left(\frac{\pi}{2}\right)\hat{\mathbf{r}}_{D_iB_i} \tag{8}$$

and $\hat{\mathbf{r}}_{D_iB_i}$ is the unit vector along $\mathbf{r}_{D_iB_i} = \mathbf{r}_{O_iB_i} - \mathbf{r}_{O_iD_i}$.

The coordinates of E_i w.r.t. F_{base} are obtained by a transformation matrix $\mathbf{A}_i^0$ as follows:

$$\mathbf{r}_{O_0E_i} = \mathbf{A}_i^0\mathbf{r}_{O_iE_i} \tag{9}$$

where

$$\mathbf{A}_i^0 = \begin{bmatrix} 0 & 0 & 1 & q_1 + (-1)^i d_{4i} \\ -\sin(\theta_i) & \cos(\theta_i) & 0 & \frac{A_{iy}+C_{iy}}{2} \\ -\cos(\theta_i) & -\sin(\theta_i) & 0 & \frac{A_{iz}+C_{iz}}{2} \\ 0 & 0 & 0 & 1 \end{bmatrix} \tag{10}$$

and θ_i, which is the angle between $\mathbf{r}_{A_iC_i}$ and the normal of the x_0y_0 plane, is calculated as follows:

$$\theta_i = \text{atan2}(y_{Ai} - y_{Ci}, z_{Ci} - z_{Ai}) \tag{11}$$

The orientation of F_{wrist} w.r.t. F_{base} is obtained from the corresponding rotation matrix $\mathbf{R}^{\text{base}}_{\text{wrist}}(\alpha,\beta,\gamma)$, where α, β and γ are the fixed XYZ Euler angles. The rotation angle along x_0 is directly obtained as $\gamma = q_{DE_1} + q_6 + \delta q_6$. According to the design of the tool part shown in Figure 2,

$$\mathbf{R}^0_{\text{wrist}}(\alpha,\beta,\gamma)\begin{bmatrix}1\\0\\0\end{bmatrix}=\frac{\mathbf{r}_{O_0F_2}-\mathbf{r}_{O_0F_1}}{||\,\mathbf{r}_{O_0F_2}-\mathbf{r}_{O_0F_1}\,||}=\begin{bmatrix}u_x\\u_y\\u_z\end{bmatrix} \tag{12}$$

Then α and β are obtained as:

$$\alpha=\sin^{-1}\left(u_y\cos\gamma+u_z\sin\gamma\right) \tag{13}$$

$$\beta=\text{atan2}\left(\ \Psi\quad\sqrt{(\cos\alpha)^2-\Psi^2}\ \right) \tag{14}$$

where, $\Psi=u_y\sin\gamma-u_z\cos\gamma$.

The translation of F_{wrist} w.r.t. F_{base} is calculated as follows:

$$\mathbf{T}^0_{\text{wrist}}=\mathbf{r}_{O_0F_1}+\mathbf{R}^0_{\text{wrist}}\begin{bmatrix}d_{41}+d_5\\0\\0\end{bmatrix} \tag{15}$$

Finally, the pose of F_{wrist} w.r.t. F_{base} is expressed as follows:

$$\mathbf{A}^0_{\text{wrist}}=\begin{bmatrix}\mathbf{R}^0_{\text{wrist}} & \mathbf{T}^0_{\text{wrist}}\\ \mathbf{0} & 1\end{bmatrix} \tag{16}$$

2.3. Force and Torque Equations

The gravity frame $F_{gravity}$ is assigned at the tool part's center of gravity, as shown in Figure 3. When the robot is not in contact with its environment, the gravity force $\mathbf{f}_G$ in frame $F_{gravity}$ is the cause of the force and torque on the force sensor. The forward kinematic solution to obtain the force and torque in force sensors is:

$$\mathbb{F}^{\text{sensor}}_{G}=\mathbb{A}^{\text{sensor}}_{\text{wrist}}\mathbb{A}^{\text{wrist}}_{\text{gravity}}\mathbb{F}^{\text{gravity}}_{G} \tag{17}$$

where $\mathbb{F}$ is a 6×1 wrench vector composed of force and torque, and $\mathbb{A}$ is a 6×6 transformation matrix between screws. The orientation of $F_{gravity}$ is in alignment with F_{world}, rather than fixed relative to the tool part. The wrench of the gravity force of the tool part w.r.t. the $F_{gravity}$ is

$$\mathbb{F}^{\text{gravity}}_{G}=\begin{bmatrix}\mathbf{f}^{\text{gravity}}_{G}\\ \mathbf{0}\end{bmatrix} \tag{18}$$

where $\mathbf{f}^{\text{gravity}}_{G}=\begin{bmatrix}0 & 0 & -m_{\text{Tool}}g\end{bmatrix}^T$ with m_{Tool} is the mass of the tool part and g is the gravitational constant. Since gravity is a pure force, $\boldsymbol{\tau}^{\text{gravity}}_{G}=\begin{bmatrix}0 & 0 & 0\end{bmatrix}^T$.

The transformation matrix $\mathbb{A}^{\text{writst}}_{\text{gravity}}$ can be expressed as

$$\mathbb{A}^{\text{writst}}_{\text{gravity}}=\begin{bmatrix}\mathbf{R}^{\text{writst}}_{\text{gravity}} & \mathbf{0}\\ \mathbf{p}^{\text{writst}}_{\text{gravity}}\times\mathbf{R}^{\text{writst}}_{\text{gravity}} & \mathbf{R}^{\text{writst}}_{\text{gravity}}\end{bmatrix} \tag{19}$$

Since $F_{gravity}$ keeps the same orientation with F_{world}, then $\mathbf{R}^{\text{wrist}}_{\text{gravity}}=\mathbf{R}^{\text{wrist}}_{\text{world}}=\left(\mathbf{R}^{\text{world}}_{\text{base}}\mathbf{R}^{\text{base}}_{\text{wrist}}\right)^T$. $\mathbf{p}^{\text{wrist}}_{\text{gravity}}=\begin{bmatrix}x_G & y_G & z_G\end{bmatrix}^T$ is the translation offset of the origin of $F_{gravity}$ w.r.t. F_{wrist}. $\mathbf{p}^{\text{wrist}}_{\text{gravity}}\times$ is the vector product operation, and it is equal to

$$\mathbf{p}_{\text{gravity}}^{\text{wrist}}\times = \begin{bmatrix} 0 & -z_G & y_G \\ z_G & 0 & -x_G \\ -y_G & x_G & 0 \end{bmatrix} \tag{20}$$

Similar to Equation (19), $\mathbb{A}_{\text{wrist}}^{\text{sensor}}$ is characterized by parameters describing F_{sensor} w.r.t. F_{wrist}:

$$\mathbb{A}_{\text{wrist}}^{\text{sensor}} = \left(\mathbb{A}_{\text{sensor}}^{\text{wrist}}\right)^{-1} = \begin{bmatrix} \left(\mathbf{R}_{\text{sensor}}^{\text{wrist}}\right)^T & \mathbf{0} \\ -\left(\mathbf{R}_{\text{sensor}}^{\text{wrist}}\right)^T \mathbf{p}_{\text{sensor}}^{\text{wrist}}\times & \left(\mathbf{R}_{\text{sensor}}^{\text{wrist}}\right)^T \end{bmatrix} \tag{21}$$

The sensor reference frame F_{sensor} is defined in the information given by the sensor manufacturer. During assembly, its orientation w.r.t. F_{wrist} is expressed by Euler-XYZ angles:

$$\mathbf{R}_{\text{sensor}}^{\text{wrist}} = \mathbf{R}_x\left(\gamma_{\text{S}}\right)\mathbf{R}_y\left(\beta_{\text{S}}\right)\mathbf{R}_z\left(\alpha_{\text{S}}\right) \tag{22}$$

Similar to Equation (20), $\mathbf{p}_{\text{sensor}}^{\text{wrist}}\times$ is the vector product operation of $\mathbf{p}_{\text{sensor}}^{\text{wrist}} = \begin{bmatrix} x_S & y_S & z_S \end{bmatrix}^T$.

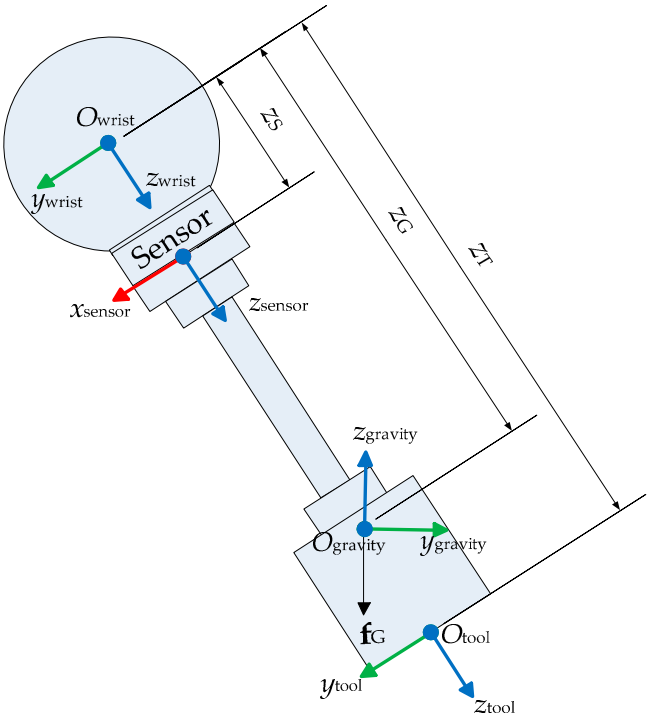

Figure 3. Gravity effect of the tool part on the force sensor.

3. Parameters Used During Calibration

In our robot calibration process, the following parameters were considered:

- The lengths of the ten links of the two five-bar mechanisms: L_{11}, L_{12}, L_{13}, L_{14}, L_{21}, L_{22}, L_{23} and L_{24}.
- The y and z coordinates of the anchor points of the two proximal links of the five-bar mechanisms: A_{1y}, A_{1z}, C_{1y}, C_{1z}, A_{2y}, A_{2z}, C_{2y}, C_{2z}.
- The offsets of the six active joints: δq_1, δq_2, δq_3, δq_4, δq_5, δq_6.
- The offset parameters for the tool part: d_{31}, d_{32}, d_{41}, d_{42}, d_5.
- The parameters defining the base with respect to the world frame: x_0, y_0, z_0, α_0, β_0, γ_0.
- The position of the tool frame with respect to the wrist frame: x_{T}, y_{T}, z_{T}, α_{T}, β_{T}, γ_{T}.
- The parameters to describe the sensor frame w.r.t. the wrist frame: x_{S}, y_{S}, z_{S}, α_{S}, β_{S}, γ_{S}.

- The parameters to describe the offset of gravity frame w.r.t. the wrist frame: x_G, y_G, z_G.
- The mass of the tool part: m_{Tool}.

Of the 46 parameters that we considerd, a total of 17 parameters are non-identifiable, which means that we need to reduce the number of identifiable parameters to 29.

4. Calibration Process

Our calibration process is explained in detail in Sections 4.1–4.3. Its main steps are presented in what follows:

1. Develop the calibration model: the forward kinematics, presented in Section 2.2.
2. Create a pool $\mathbf{\Omega}$ of 40,000 configurations uniformly distributed inside the whole robot workspace. Create a set $\mathbf{\Omega}_t$ of 336 configurations uniformly distributed inside the target workspace (see Section 4.3). We note that the configurations of the set $\mathbf{\Omega}_t$ are different from these of $\mathbf{\Omega}$.
3. Select 100 configurations to be used in the identification process. These configurations are chosen through an observability analysis, as explained in Section 4.1.
4. Take the force and torque measurements, for all robot configurations ($\mathbf{\Omega}_t$ and $\mathbf{\Omega}$). Measurements are done by using the robot force-torque sensor. We note that in this paper all measurements are generated by simulation, as explained in Sections 4.3 and 5.
5. Identify the robot parameter values by using the calibration configurations selected in step 3; the identification approach is presented in details in Section 4.2.
6. Evaluate the accuracy after calibration, as explained in Section 5.

4.1. Selection of Calibration Configurations

After creating the calibration model, and generating a pool $\mathbf{\Omega}$ of 40,000 configurations uniformly distributed inside the whole robot workspace, a set of 100 calibration configurations is selected among $\mathbf{\Omega}$. This is done by using an approach commonly called *observability analysis*. This analysis is used to obtain the optimal set of the calibration configurations, and is based on the singular value decomposition (SVD) of the *identification Jacobian matrix* $\mathbf{J}$. The matrix $\mathbf{J}$ is composed of the derivatives of the end-effector force and torque vector (Equation (17)), with respect to all of the robot independent parameters. The Jacobian matrix is also used in the linearization of the force and torque equations (Equation (17)), around the calibration configurations (*i.e.*, Taylor approximation). This linearization allows identifying the parameter values, as explained in Section 4.2. The nominal values of the robot's independent parameters are represented by the vector $\mathbf{p_{nom}}$. The matrix $\mathbf{J}$ is calculated as follows, for $i = 1 \ldots n$.

$$\mathbf{J} = \begin{bmatrix} \mathbf{J}_1 \\ \vdots \\ \mathbf{J}_n \end{bmatrix} \tag{23}$$

where J_i is the $6 \times m$ Jacobian matrix at the ith calibration configuration, n is the number of calibration configurations, and m is the number of considered parameters (not all of which are necessarily identifiable). In our case, $n = 100$ and $m = 49$.

$\mathbf{J}_\mathrm{i}$ is given by:

$$\mathbf{J}_i = \begin{bmatrix} \frac{\partial F_{x,i}}{\partial \mathbf{p}_{\mathrm{nom}}} \\ \frac{\partial F_{y,i}}{\partial \mathbf{p}_{\mathrm{nom}}} \\ \frac{\partial F_{z,i}}{\partial \mathbf{p}_{\mathrm{nom}}} \\ \frac{\partial T_{x,i}}{\partial \mathbf{p}_{\mathrm{nom}}} \\ \frac{\partial T_{y,i}}{\partial \mathbf{p}_{\mathrm{nom}}} \\ \frac{\partial T_{z,i}}{\partial \mathbf{p}_{\mathrm{nom}}} \end{bmatrix} \tag{24}$$

The matrix **J** is also used to find the non-identifiable parameters. The rank r_J of the Jacobian **J** represents the number of identifiable parameters. If $r_J < m$, then $m - r_J$ parameters are non-identifiable; the corresponding columns should be removed from **J**. This procedure is carried out using an algorithm that is based on the approach proposed in [21]. The stop criteria is when m becomes equal to r_J. The algorithm proceeds as follows:

1. Remove all zero columns from **J**. The corresponding parameters have no impact on the calibration model.
2. Calculate the condition number, c_J, of J. The condition number is used to evaluate how good is the matrix **J** for the parameter identification. With a bad condition number (high value), the solutions are unstable with respect to small changes in measurement errors. Therefore, to have a robust identification system, the condition number should be as small as possible.
3. Remove, one at a time, the column related to each parameter from **J**, and calculate both the new rank and condition number (r_J^* and c_J^*) for the new Jacobian matrix $\mathbf{J}^*$. The column that, if eliminated, results in the maximum reduction of the condition number and gives the same rank ($r_J^* = r_J$), is definitively removed (*i.e.*, the corresponding parameter will be not subject to the identification process).
4. Replace **J** with **J***, and repeat the process from step (2).

As a result, of the 49 parameters considered in our calibration model, 22 are non-identifiable and are indicated by the symbol '*' in Table 1.

The fact that some parameters are non-identifiable is mainly due to redundancy, or the fact that they have no impact on the force and torque equations that represent the calibration model.

The parameter identification is achieved by minimizing the residual of the end-effector force and torque, which are measured by the robot's force sensor (Figure 3); no external measurement device is required. Further, only the gravity effect of the end-effector is used to apply forces to the robot's end-effector. Therefore, to change the applied force on the end-effector, it is necessary to change its orientation.

In our identification process, 100 calibration configurations are selected from among the 40,000 configurations. The remaining 39,900 configurations are used for validation purpose. The 40,000 configurations are uniformly distributed on three layers, within the entire robot workspace. Note that several orientations are generated for each position. The calibration configurations are selected using an observability analysis, which allows us to identify the most appropriate configurations and thus identify the most effective parameters. This analysis is based on using the first observability index, denoted by O_1 and calculated by using the singular value of the Jacobian identification matrix (*i.e.*, the sensitivity matrix). The procedure of selecting the calibration configurations is based on the DETMAX algorithm, which was initially proposed in [24].

According to [25,26], the index O_1 seems to be the most appropriate index for the kinematic calibration. This was also confirmed by our simulation, through a comparison of the five observability indices that were presented in the literature and thoroughly detailed in [26]. The convergence of O_1 is represented in Figure 4, and is calculated as follows:

$$O_1 = \frac{(\sigma_1 \sigma_2 \dots \sigma_m)^{\frac{1}{m}}}{\sqrt{n}} \tag{25}$$

where n is the number of calibration configurations, $\sigma_1 \dots \sigma_m$ are the singular values of the Jacobian identification matrix for the $m = 29$ identifiable parameters.

Table 1. Results of the simulated parameter identification.

Param.	Nom.	Actual	Identified, without Meas. Errors	Identified, with Meas. Errors
A_{1y} (mm)	−233.000	−233.000	−233.000	−233.000
A_{1z} (mm)	178.000	178.612	178.612	178.659
C_{1y} (mm)	−83.000	−84.005	−84.005	−84.002
C_{1z} (mm)	438.000	438.000	438.000	438.000
A_{2y} (mm)	−233.000	−232.267	−232.267	−232.294
A_{2z} (mm)	178.000	177.325	177.325	177.485
C_{2y} (mm) *	−83.000	−83.000	−83.000	−83.000
C_{2z} (mm)	438.000	438.112	438.112	438.210
L_{11} (mm)	400.000	400.730	400.730	400.742
L_{12} (mm)	520.000	520.221	520.221	520.321
L_{13} (mm)	400.000	398.485	398.485	398.502
L_{14} (mm)	520.000	520.332	520.332	520.271
L_{21} (mm)	400.000	399.799	399.799	399.774
L_{22} (mm)	520.000	518.336	518.336	518.505
L_{23} (mm) *	400.000	400.000	400.000	400.000
L_{24} (mm)	520.000	520.445	520.445	520.460
d_{41} (mm)	41.500	41.660	41.660	41.657
d_{42} (mm) *	41.500	41.500	41.500	41.500
d_5 (mm) *	0.000	0.000	0.000	0.000
x_T (mm) *	0.000	0.000	0.000	0.000
y_T (mm) *	0.000	0.000	0.000	0.000
z_T (mm) *	134.600	134.600	134.600	134.600
α_T (°) *	67.512	67.512	67.512	67.512
β_T (°) *	0.000	0.000	0.000	0.000
γ_T (°) *	0.000	0.000	0.000	0.000
x_0 (mm) *	109.000	109.000	109.000	109.000
y_0 (mm) *	139.000	139.000	139.000	139.000
z_0 (mm) *	−31.000	−31.000	−31.000	−31.000
α_0 (°) *	0.000	0.000	0.000	0.000
β_0 (°)	0.000	0.525	0.525	0.531
γ_0 (°)	0.000	−0.134	−0.134	−0.176
δq_2 (°)	0.000	0.313	0.313	0.342
δq_3 (°)	0.000	−0.052	−0.052	−0.014
δq_4 (°)	0.000	0.500	0.500	0.529
δq_5 (°)	0.000	0.135	0.135	0.173
δq_6 (°)	0.000	0.102	0.102	0.097
x_S (mm) *	41.500	41.500	41.500	41.500
y_S (mm) *	0.000	0.000	0.000	0.000
z_S (mm) *	41.700	41.700	41.700	41.700
α_S (°)	−67.512	−67.397	−67.397	−67.430
β_S (°)	0.000	−0.525	−0.525	−0.528
γ_S (°)	0.000	0.185	0.185	0.196
x_G (mm)	0.000	0.576	0.576	0.571
y_G (mm)	0.000	0.059	0.059	0.042
z_G (mm)	152.400	153.132	153.132	153.136
m_{Tool} (g)	0.365	0.365	0.365	0.365

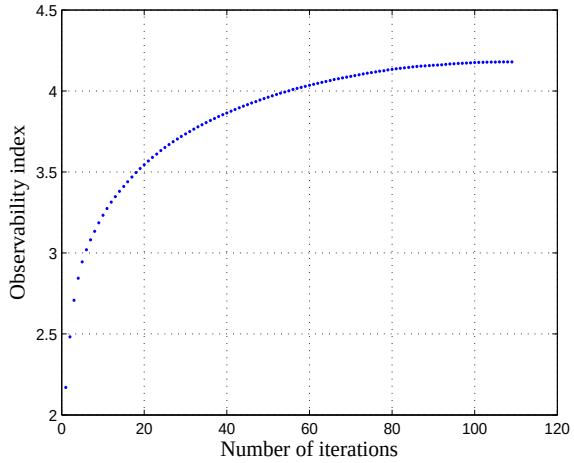

Figure 4. Evolution of the observability index O_1 with respect to the selection algorithm iterations.

4.2. Parameter Identification Process

The parameter identification process is based on using the Jacobian matrix **J**, which relates the force and torque errors to the 29 unknown parameter values. The matrix **J** is built by the linearization of the forward kinematics model (Equation (17)) around each calibration configuration. The parameter values are identified by means of an iterative algorithm, in which the parameters' vector is initialized by $\mathbf{p_{nom}}$, and is updated at each iteration (*i.e.*, replaced by the vector $\mathbf{p}_{\text{identified}}$ of the identified values). The matrix **J** is also iteratively updated, since its calculation is based on **p**.

The identification algorithm is presented in Figure 5 and has the following steps:

(a) Matrix **J** is calculated, as explained in Section 4.1. This calculation involves **p** and the values of the vector $\boldsymbol{\psi_i} = [q_1, q_2, \ldots, q_6]^{\mathrm{T}}$ $(i = 1, \ldots, n)$ of active joints of the 100 calibration configurations.

(b) A system of linear equations is formed by the measured force and torque errors, the unknown robot's parameter errors, and the Jacobian matrix **J**. In order to maintain acceptable variance of each parameter (*i.e.*, proper convergence in the linear system), parameter scaling is implemented, by using the column scaling approach proposed in [24]. The scaled matrix obtained is denoted by $\mathbf{J}_{\text{scal}}$, and it is used to identify the robot's scaled parameter errors ($\boldsymbol{\Delta}_{scal}$), as follows:

$$\boldsymbol{\Delta}_{scal} = \left(\mathbf{J}_{scal}^{T}\mathbf{J}_{scal}\right)^{-1}\mathbf{J}_{scal}^{T}\begin{bmatrix} Fx_{meas,1} - Fx_{est,1} \\ Fy_{meas,1} - Fy_{est,1} \\ Fz_{meas,1} - Fz_{est,1} \\ Tx_{meas,1} - Tx_{est,1} \\ Ty_{meas,1} - Ty_{est,1} \\ Tz_{meas,1} - Tz_{est,1} \\ \vdots \\ Fx_{meas,n} - Fx_{est,n} \\ Fy_{meas,n} - Fy_{est,n} \\ Fz_{meas,n} - Fz_{est,n} \\ Tx_{meas,n} - Tx_{est,n} \\ Ty_{meas,n} - Ty_{est,n} \\ Tz_{meas,n} - Tz_{est,n} \end{bmatrix} \tag{26}$$

where, $[Fx_{meas,i}, Fy_{meas,i}, Fz_{meas,i}, Tx_{meas,i}, Ty_{meas,i}, Tz_{meas,i}]^{\mathrm{T}}$ is the vector of the measured force and torque i, and $[Fx_{est,i}, Fy_{est,i}, Fz_{est,i}, Tx_{est,i}, Ty_{est,i}, Tz_{est,i}]^{\mathrm{T}}$ is the corresponding estimated vector. The estimated vector is calculated by substituting in the forward kinematic equation (Equation (17)): The vector **p** of the parameters' values and the vector $\boldsymbol{\psi_i}$ of the active joint variables. The vector **p** is initialized by its nominal values $\mathbf{p_{nom}}$, and updated after each iteration of this identification algorithm.

(c) The parameter errors, which represent the difference between the real values and the nominal values of the parameters, are denoted by $\boldsymbol{\Delta}$, and calculated as follows:

$$\boldsymbol{\Delta} = diag\left(D_1, D_2, \cdots, D_m\right)^{-1}\boldsymbol{\Delta}_{scal} \tag{27}$$

where D_j, $(j = 1, 2, \ldots, m)$ are the scaling coefficients, defined as follows: $D_j = \sqrt{\sum_{i=1}^{6n}\mathbf{J}_{i,j}^2}$. Also, n is the number of calibration configurations, and $\mathbf{J}_{ij}$ is the element of the Jacobian matrix located at the ith row and the jth column.

(d) Finally, the vector of the identified parameter values is

$$\mathbf{p}_{identified} = \mathbf{p}_{\text{nom}} + \boldsymbol{\Delta} \tag{28}$$

To converge towards a solution for the unknown parameter values, an iterative Newton-based procedure was used. After $\mathbf{p}_{\text{identified}}$ has been calculated, the $\mathbf{p}$ vector is replaced by the last $\mathbf{p}_{\text{identified}}$ vector obtained, and the estimation process is restarted from step (a).

Steps (a) to (d) are repeated until reaching a convergence criterion, which is the root mean square error (*RMSE*) between two successive iterations. The *RMSE* is evaluated between the vector of the latest identified parameters and the previous one. The convergence criterion was set to 10^{-16}, and the system converged towards a solution after five iterations.

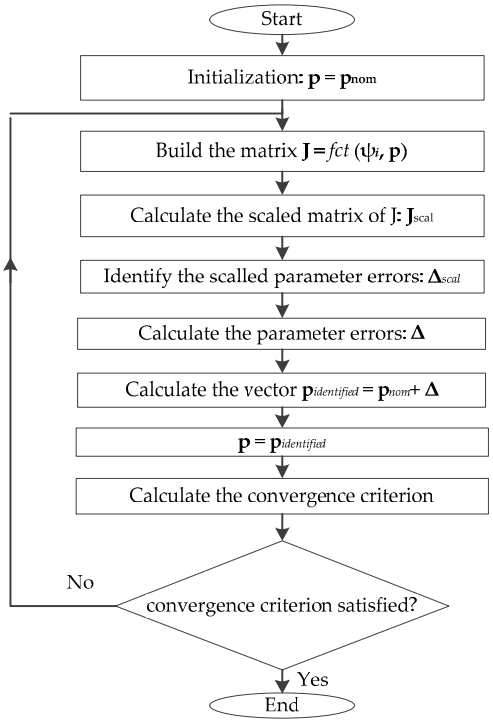

Figure 5. Flow chart of the parameter identification algorithm.

4.3. Validation after Calibration

After calibration, the accuracy is validated using 336 configurations that are uniformly distributed inside the Cartesian target workspace. The target workspace is intended to correspond to the area where the patient's leg will be located (Figure 6b). Also, the accuracy after calibration is evaluated by using the 39,900 configurations (denoted by $\mathbf{\Omega_w}$), which are the remaining configurations among the initial set $\mathbf{\Omega}$ composed of 40,000 configurations (Figure 6a) uniformly distributed within the whole robot workspace: 100 calibration configurations are selected from $\mathbf{\Omega}$, through the observability analysis, to be used in the parameter identification process, and 39,900 configurations are used in the validation after calibration.

After achieving the parameter identification process, the identified parameters are used in the robot kinematics, instead of the nominal parameter values. The next step consists to evaluate the robot accuracy for all validation configurations ($\mathbf{\Omega_w}$ and $\mathbf{\Omega_t}$), by using the following algorithm:

Loop 1

For each validation set, $\mathbf{\Omega_w}$ and $\mathbf{\Omega_t}$:

Loop 2

For each validation configuration:

(a) Calculate the desired position, by using the identified parameter values and the active joint angles $\psi = [q_1, q_2, \ldots, q_6]^T$ of the validation configuration. The end-effector position is the translation vector of the homogeneous matrix presented in Equation (1).

(b) Calculate the actual position, by using the actual parameter values (generated by simulation) and the active joint angles of the calibration validation. In case of experimental tests, the actual position is obtained by measurement.

(c) Calculate x, y, and z position errors (Ex, Ey, and Ez), by evaluating the difference between the desired and the actual position, obtained in steps (a) and (b), respectively.

(d) Calculate the composed error ($\sqrt{Ex^2 + Ey^2 + Ez^2}$) by using results obtained in step (c).

End Loop 2

Calculate the mean, the maximum and the standard deviation of all composed errors obtained in *Loop* 1.

End Loop 1

The force and torque validation is achieved by using the same algorithm as for position. The only difference is using Equation (17) instead of Equation (1), in step (a).

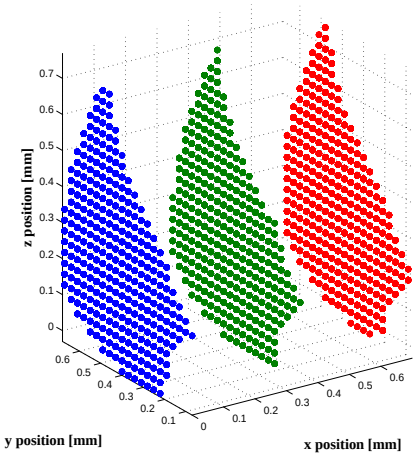

(**a**)

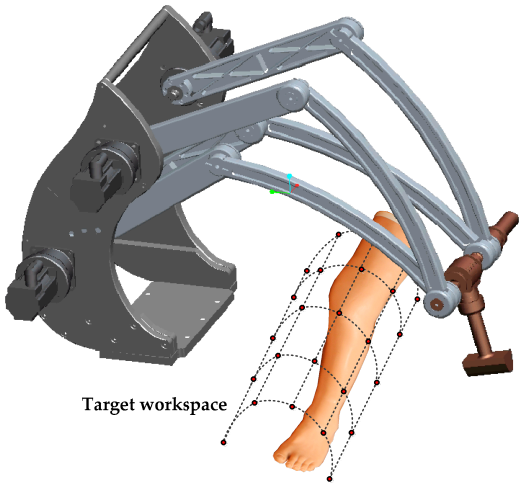

(**b**)

Figure 6. The positioning of the robot end-effector within (**a**) the whole robot workspace; 40,000 configurations inside the whole robot workspace; and (**b**) the target workspace; 336 configurations inside the area where the patient's leg will be located.

5. Simulation Study

The efficiency of our calibration process is evaluated through a simulation. This process also evaluates the sensitivity of our identification process to the measurement noise, and verifies the effectiveness of the observability analysis for choosing the calibration configurations. Finally, the calibration results (*i.e.*, position accuracy) that were obtained from each of the five observability indices are compared, and the index that gives the best accuracy is used in the actual calibration.

For simulation purposes, the actual parameters' values are simulated by introducing randomly-generated errors of ± 2 mm for the distances, and $\pm 1^{\circ}$ for the angles. The differences between the nominal and the actual parameter errors simulate the behavior of a robot with poor accuracy. By using the calibration process, the identified parameters will be as close as possible to their actual values, despite the presence of the measurement errors. The measurement errors that were used in our simulation are $\pm$ 1 N and $\pm$ 0.2 N$\cdot$ m, for the force and torque, respectively. These errors are an exaggeration of the accuracy of the robot's force-torque sensor (a Mini 40 from ATI), the details of which are provided by its manufacturer, through a calibration certificate. From this information, force accuracy according to x, y, and z axes was $\pm$ 0.25 N, $\pm$ 0.2 N, and $\pm$ 0.45 N, respectively. The torque accuracy was $\pm$ 0.0125 N.m, $\pm$ 0.0125 N.m, and $\pm$ 0.02 N.m, for x, y, and z axes.

The measurement errors are generated according to a normal distribution, for each axis (*i.e.*, errors for F_x are generated within $\pm$ 1 N, and similarly for F_y and F_z). The data acquisition is simulated by generating 100 measurements (*i.e.*, force and torque errors) for each calibration configuration of the robot. As it is known that the number of identifiable parameters is 29, the number of calibration configurations that are used in the identification process is 100, in order to over-constrain the calibration model.

The measured wrench vector (composed of force and torque) is simulated for each calibration configuration, by substituting the corresponding active joint angles and the actual parameter values (Table 1) in Equation (17). A vector of measurement noise is then added to the obtained wrench vector.

Once all force-torque vectors are generated, the robot parameters are identified as explained in Section 4.2. The identified parameter values are presented in Table 1.

Once the parameters have been identified, the calibration process is validated. This validation is carried out, as explained in Section 4.3, on two levels: the robot's position accuracy is assessed in both the whole robot workspace (39,900 configurations) and by using the 336 positions that are uniformly distributed within the target workspace. The force, torque and position errors are summarized in Table 2 and Table 3, and it shows that the position accuracy was improved from 8.9135 mm before calibration to 286 µm, after calibration, inside the target workspace. The wrench errors (Table 4) were highly improved (better than the position accuracy improvement) because in our identification process, only the residuals of force and torque were minimized in the objective function Equation (26). The distribution of the robot's position errors (before and after calibration) is presented in Figure 7 and Figure 8, which represent the number of occurrences (frequency) of robot xyz composed position errors that lie within the ranges of error, presented on the horizontal axis.

A deep analysis of the position errors, for the whole workspace, shows that 0.33% of the evaluated positions have an accuracy lower than 0.2024 mm (mean $-$ 2 $\times$ STD), 94.37% are within the range mean $\pm$ 2 $\times$ STD, and only 5.3% of positions present the poorer accuracy, which is higher than 0.3696 (mean + 2 $\times$ STD). The same analysis was achieved for the target workspace, and it shows that 93.0952% of positions have an accuracy within 0.2457 mm and 0.3085 mm (mean $\pm$ 2 $\times$ STD), and only 6.9048% of positions have errors higher than 0.3085 mm (mean + 2 $\times$ STD).

For illustrative purpose, Table 4 shows the accuracy obtained by using each observability index, separately, in the calibration process. Results confirm that O_1 is the most appropriate index for calibrating our robot, since it gives the smallest position (and force/torque) errors, after calibration. Moreover, deeper statistical analyses were carried out on the results obtained by the five indices. First we verified whether the data distributions are Gaussian or not, and then used parametric or non-parametric tests accordingly. Therefore a Kolmogorov-Smirnov test (not shown) was achieved,

and it showed that all observability indices provide Gaussian distribution. Based on these results, we decided to use parametric analyses (*i.e.*, ANOVA analysis, and *t-test*).

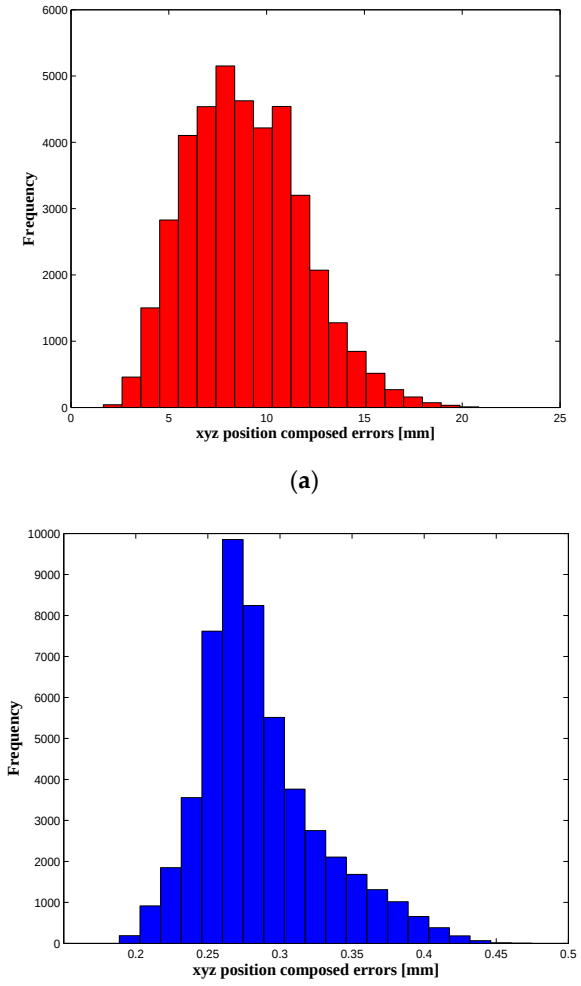

Figure 7. Position errors in the whole workspace (**a**) before and (**b**) after calibration.

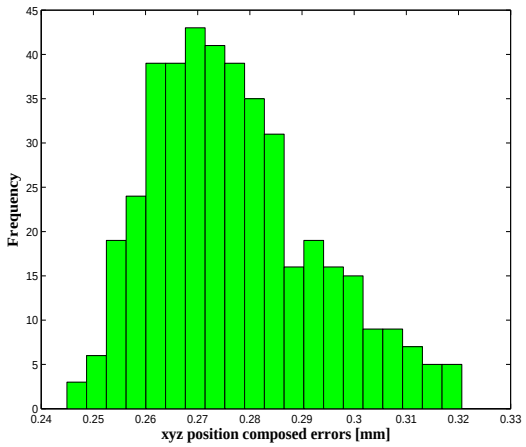

Figure 8. Position errors in the target workspace after calibration.

Table 2. Composite force and torque errors before and after calibration.

	Force (N)				Torque (N.m)			
	Mean	**Mean % w.r.t. Max**	**Max**	**STD**	**Mean**	**Mean % w.r.t. Max**	**Max**	**STD**
				Whole Workspace				
Before	0.0703	24.84	0.2830	0.0454	0.0100	28.33	0.0353	0.0056
After	0.0004	20.00	0.0020	0.0003	0.0000	0.00	0.0002	0.0000
Improvement %	99.43	-	99.29	99.34	100.00	-	99.43	100.00
				Target Workspace				
Before	0.0474	46.33	0.1023	0.0264	0.0055	60.44	0.0091	0.0018
After	0.0008	61.54	0.0013	0.0002	0.0002	66.67	0.0003	0.0000
Improvement %	98.31	-	98.73	99.24	96.36	-	96.70	100.00

Table 3. Composite position errors before and after calibration.

	Mean (mm)	**Mean% w.r.t. Max**	**Max (mm)**	**STD (mm)**
		Whole Workspace		
Before	8.9135	42.76	20.8437	2.9138
After	0.2860	60.24	0.4748	0.0418
Improvement %	96.79	-	97.72	98.57
		Target Workspace		
Before	9.0118	73.64	12.2382	1.6537
After	0.2771	86.43	0.3206	0.0157
Improvement %	96.93	-	97.38	99.05

Table 4. Composite force, torque and position errors after calibration using the five observability indices.

	Force (N)			Torque (N.m)			Position (mm)		
	Mean	**Max**	**STD**	**Mean**	**Max**	**STD**	**Mean**	**Max**	**STD**
					Whole Workspace				
O_1	0.0004	0.0020	0.0003	0.0000	0.0002	0.0000	0.2860	0.4748	0.0418
O_2	0.0024	0.0189	0.0031	0.0003	0.0021	0.0003	0.3818	0.9391	0.1070
O_3	0.0644	0.0497	0.1011	0.0114	0.0553	0.0112	8.8182	10.1284	0.4050
O_4	0.0122	0.0356	0.0099	0.0013	0.0040	0.0011	4.5199	6.2311	0.3134
O_5	0.0006	0.0031	0.0004	0.0001	0.0003	0.0000	0.4552	0.6767	0.0637
					Target Workspace				
O_1	0.0005	0.0012	0.0002	0.0001	0.0001	0.0000	0.2771	0.3206	0.0157
O_2	0.0008	0.0014	0.0003	0.0002	0.0003	0.0000	0.3527	0.4493	0.0231
O_3	0.0387	0.0569	0.0282	0.0025	0.0043	0.0052	7.5427	10.7637	0.7089
O_4	0.0124	0.0228	0.0047	0.0013	0.0025	0.0005	4.4836	5.8925	0.1638
O_5	0.0003	0.0008	0.0001	0.0000	0.0001	0.0000	0.4318	0.5937	0.0320

Initially, an ANOVA analysis, with a probability threshold $\alpha = 0.05$, is used to confirm the objectivity of comparing the five indices (*i.e.*, confirm that there is actually differences between the use of the five indices). Results show that the *F value* is significantly higher than the *F criteria*, which leads to reject the null hypothesis, and therefore conclude that the comparison of results (position accuracy) obtained by using the five indices is meaningful (*i.e.*, results are different, and some indices are better than others).

The ANOVA does not tell where the difference between indices lies. Therefore, an additional test is considered (*t-test*). The *t-test* is used to compare each pair of indices. However, the position errors obtained by using O_3 and O_4 were clearly poorer than results obtained by the other indices (O_1, O_2, and O_5). Thus, only O_1, O_2, and O_5 are considered in the *t-Test*. The results of this test are shown in Table 5,

and they show that the position errors obtained by these three indices are quite different, since the *t Stat* value is significantly lower than –*t_Critical_two-tail*, for all pairs of comparisons. Furthermore, to take into account multiple comparison effects, a post-hoc correction is included (Bonferroni correction). As summarized in Table 5, results show that all the *t*-tests were statistically significant (*i.e.*, there are significant differences between the performances of the observability indices).

Table 5. Results of the *t*-test comparing pairs of O_1, O_2, and O_5.

***t*-Test**			
	O_1 *vs.* O_2	O_1 *vs.* O_5	O_2 *vs.* O_5
t Stat	−655.874	−304.773	421.3063
t Critical two-tail	1.960001	1.959993	1.959993
Post-hoc correction (Bonferroni correction) ***Target p-value*** **=** $\frac{\alpha}{\text{number of t-Test}} = \frac{0.05}{3} = 0.0167$			
p-value(from t-test)	0.000000	0.000000	0.000000
Test statistically significant	yes	yes	yes

Based on the aboves tests, we conclude that the fives observability indices allow different results, regarding the robot accuracy after calibration. The analysis of the mean and maximum errors (Table 4) shows that the index O_1 leads to the best robot accuracy: it gives not only the smallest mean errors, but also the smallest maximum errors. Also, O_1 has a small standard deviation, which means that position errors are closely distributed around the mean value.

We recall that in our simulation the used measurement noise was ± 1 N. This range of error is an exaggerated error of our wrench sensor (Mini 40, from *API*). For illustrative propose, we achieved other simulations by considering lower measurement noise (Table 6). Results demonstrate that the accuracy after calibration is much better in case of low measurement errors. However, the impact of these errors can be reduced by:

- Using continuous tracking approach: taking several measurements for each robot calibration configuration (*i.e.*, the same applied force), and then averaging the collected data. Most sensors, and data collection card allow a frequency upper than 100 Hz.
- Calibrating the wrench sensor only in a limited range, in which the sensor will be actually used. This will reduce the measurement uncertainty.

Table 6. Composite position errors after calibration, inside the target workspace, using different measurement errors.

Err. (N)	Mean	Max	STD
$\pm$**0.2**	0.0759	0.0885	0.0039
$\pm$**0.4**	0.1124	0.1992	0.0042
$\pm$**0.6**	0.1874	0.2845	0.0070
$\pm$**0.8**	0.2174	0.3014	0.0103
$\pm$**1**	0.2771	0.3206	0.0157

6. Conclusions

We have presented a self-kinematic calibration approach using a force-torque sensor. With this approach, the position accuracy of a 6-DOF medical robot was significantly improved. The robustness of our calibration model, regarding measurement noise, was confirmed through a simulation study, which also allowed us to conduct an observability analysis in order to identify the most appropriate calibration configurations. The simulation demonstrated that the robot's position errors were reduced

from 12 mm to 0.320 mm for the maximum values, and from 9 mm to 0.277 mm for the mean errors. The calibration method presented in this paper will be tested experimentally in further work.

Acknowledgments: We thank the Canada Research Chairs program for funding this work.

Author Contributions: Ahmed Joubair designed and carried out the calibration study, and wrote the paper; Long Fei Zhao and Pascal Bigras, developed the robot kinematics; Ilian A. Bonev supervised the project.

Conflicts of Interest: The authors declare no conflict of interest.

References

1. Beasley, R.A. Medical robots: Current systems and research directions. *J. Robot.* **2012**, *2012*. [CrossRef]
2. Speich, J.E.; Rosen, J. Medical robotics. In *Encyclopedia of Biomaterials and Biomedical Engineering*; CRC Press: Boca Raton, FL, USA, 2004; pp. 983–993.
3. Zhao, L.; Yen, A.K.W.; Coulombe, J.; Bigras, P.; Bonev, I.A. Kinematic analyses of a new medical robot for 3D vascular ultrasound examination. *Trans. Can. Soc. Mech. Eng.* **2013**, *38*, 227–239.
4. Vieyres, P.; Poisson, G.; Courrèges, F.; Smith-Guerin, N.; Novales, C.; Arbeille, P. A Tele-Operated Robotic System for Mobile Tele-Echography: The Otelo Project. In *M-Health: Emerging Mobile Health Systems*; Istepanian, R.S.H., Laxminarayan, S., Pattichis, C.S., Eds.; Springer US: New York, NY, USA, 2006; pp. 461–473.
5. Pierrot, F.; Dombre, E.; Dégoulange, E.; Urbain, L.; Caron, P.; Gariépy, J.; Mégnien, J.L. Hippocrate: A safe robot arm for medical applications with force feedback. *Med. Image Anal.* **1999**, *3*, 285–300. [CrossRef]
6. Broeders, I.A.M.J.; Ruurda, J. Robotics revolutionizing surgery: The Intuitive Surgical "Da Vinci" system. *Ind. Robot Int. J.* **2001**, *28*, 387–392. [CrossRef]
7. Shimachi, S.; Hirunyanitiwatna, S.; Fujiwara, Y.; Hashimoto, A.; Hakozaki, Y. Adapter for contact force sensing of the da Vinci® robot. *Int. J. Med. Robot. Comput. Assist. Surg.* **2008**, *4*, 121–130. [CrossRef] [PubMed]
8. Schulz, A.P.; Seide, K.; Queitsch, C.; von Haugwitz, A.; Meiners, J.; Kienast, B.; Tarabolsi, M.; Kammal, M.; Jürgens, C. Results of Total Hip Replacement Using the Robodoc Surgical Assistant System: Clinical Outcome and Evaluation of Complications for 97 Procedures. *Int. J. Med. Robot. Comput. Assist. Surg.* **2007**, *3*, 301–306. [CrossRef] [PubMed]
9. Hogan, N.; Krebs, H.I.; Charnnarong, J.; Srikrishna, P.; Sharon, A. MIT-MANUS: A workstation for manual therapy and training. I. In Proceedings of the IEEE International Workshop on Robot and Human Communication, Tokyo, Japan, 1–3 September 1992; pp. 161–165.
10. Krebs, H.I.; Ferraro, M.; Buerger, S.P.; Newbery, M.J.; Makiyama, A.; Sandmann, M.; Lynch, D.; Volpe, B.T.; Hogan, N. Rehabilitation robotics: Pilot trial of a spatial extension for MIT-Manus. *J. NeuroEng. Rehabil.* **2004**, *1*, 5. [CrossRef] [PubMed]
11. Galvez, J.A.; Reinkensmeyer, D.J. Robotics for gait training after spinal cord injury. *Top. Spinal Cord Inj. Rehabil.* **2005**, *11*, 18–33. [CrossRef]
12. Otr, O.V.D.N.; Reinders-Messelink, H.A.; Bongers, R.M.; Bouwsema, H.; van der Sluis, C.K. The i-LIMB hand and the DMC plus hand compared: A case report. *Prosthet. Orthot. Int.* **2010**, *34*, 216–220. [PubMed]
13. Low, K. Robot-assisted gait rehabilitation: From exoskeletons to gait systems. In Proceedings of the Defense Science Research Conference and Expo (DSR), Singapore, 3–5 August 2011; pp. 1–10.
14. Joubair, A.; Slamani, M.; Bonev, I.A. Kinematic calibration of a 3-DOF planar parallel robot. *Ind. Robot* **2012**, *39*, 392–400. [CrossRef]
15. Joubair, A.; Slamani, M.; Bonev, I.A. Kinematic calibration of a five-bar planar parallel robot using all working modes. *Robot. Comput. Integr. Manuf.* **2013**, *29*, 15–25. [CrossRef]
16. Joubair, A.; Nubiola, A.; Bonev, I.A. Calibration efficiency analysis based on five observability indices and two calibration models for a six-axis industrial robot. *SAE Int. J. Aerosp.* **2013**, *6*, 161–168. [CrossRef]
17. Nubiola, A.; Slamani, M.; Joubair, A.; Bonev, A.I. Comparison of two calibration methods for a small industrial robot based on an optical CMM and a laser tracker. *Robotica* **2013**, *32*, 447–466. [CrossRef]
18. Joubair, A.; Bonev, I.A. Absolute accuracy analysis and improvement of a hybrid 6-DOF medical robot. *Ind. Robot* **2015**, *42*, 44–53. [CrossRef]
19. Kim, H.S. Kinematic calibration of a Cartesian parallel manipulator. *Int. J. Control Autom. Syst.* **2005**, *3*, 453–460.

20. Huang, T.; Hong, Z.Y.; Mei, J.P.; Chetwynd, D.G. Kinematic calibration of the 3-DOF module of a 5-DOF reconfigurable hybrid robot using a double-ball-bar system. In Proceedings of the IEEE/RSJ International Conference on Intelligent Robots and Systems, Beijing, China, 9–15 October 2006; pp. 508–512.
21. Joubair, A.; Bonev, I.A. Kinematic calibration of a six-axis serial robot using distance and sphere constraints. *Int. J. Adv. Manuf. Technol.* **2014**, *77*, 515–523. [CrossRef]
22. Joubair, A.; Bonev, I.A. Non-kinematic calibration of a six-axis serial robot using planar constraints. *Precis. Eng.* **2015**, *40*, 325–333. [CrossRef]
23. Gabiccini, M.; Stillfried, G.; Marino, H.; Bianchi, M. A data-driven kinematic model of the human hand with soft-tissue artifact compensation mechanism for grasp synergy analysis. In Proceedings of the IEEE/RSJ International Conference on Intelligent Robots and Systems—IROS, Tokyo, Japan, 3–7 November 2013.
24. Mitchell, T.J. An algorithm for the construction of D-optimal experimental designs. *Technometrics* **1974**, *42*, 203–210.
25. Sun, Y.; Hollerbach, J. Observability index selection for robot calibration. In Proceedings of the IEEE International Conference on Robotics and Automation, Pasadena, CA, USA, 19–23 May 2008.
26. Joubair, A.; Bonev, I.A. Comparison of the efficiency of five observability indices for robot calibration. *Mech. Mach. Theory* **2013**, *70*, 254–265. [CrossRef]